






## Article

# Long-Term Stability of TiS<sub>2</sub>–Alkylamine Hybrid Materials

Federica Ursi <sup>1</sup>, Simone Virga <sup>1</sup>, Gonzalo García-Espejo <sup>2</sup>, Norberto Masciocchi <sup>2</sup>, Antonino Martorana <sup>1</sup>  
and Francesco Giannici <sup>1,\*</sup>

<sup>1</sup> Dipartimento di Fisica e Chimica—Emilio Segrè, Università di Palermo, Viale delle Scienze, 90128 Palermo, Italy

<sup>2</sup> Dipartimento di Scienza e Alta Tecnologia and To.Sca.Lab., Università dell'Insubria, Via Valleggio 11, 22100 Como, Italy

\* Correspondence: francesco.giannici@unipa.it

**Abstract:** Layered TiS<sub>2</sub> intercalated with linear alkylamines has recently attracted significant interest as a model compound for flexible *n*-type thermoelectric applications, showing remarkably high power factors at room temperature. The thermal and, particularly, environmental stability of such materials is, however, a still an open challenge. In this paper, we show that amine-intercalated TiS<sub>2</sub> prepared by a simple mechanochemical process is prone to chemical decomposition through sulfur exsolution, and that the presence of molecular oxygen is likely to mediate the decomposition reaction. Through computational analysis of the possible reaction pathways, we propose that Ti-N adducts are formed as a consequence of amine groups substituting for S vacancies on the internal surfaces of the S-Ti-S layers. These findings provide insights for possible future applications of similar hybrid compounds as devices operating in ambient conditions, and suggest isolating them from atmospheric oxygen.

**Keywords:** chalcogenides; thermoelectrics; X-ray diffraction; Raman; intercalation



**Citation:** Ursi, F.; Virga, S.; Garcia-Espejo, G.; Masciocchi, N.; Martorana, A.; Giannici, F. Long-Term Stability of TiS<sub>2</sub>–Alkylamine Hybrid Materials. *Materials* **2022**, *15*, 8297. <https://doi.org/10.3390/ma15238297>

Academic Editor: Mario Culebras Rubio

Received: 24 October 2022

Accepted: 18 November 2022

Published: 22 November 2022

**Publisher's Note:** MDPI stays neutral with regard to jurisdictional claims in published maps and institutional affiliations.



**Copyright:** © 2022 by the authors. Licensee MDPI, Basel, Switzerland. This article is an open access article distributed under the terms and conditions of the Creative Commons Attribution (CC BY) license (<https://creativecommons.org/licenses/by/4.0/>).

## 1. Introduction

Thermoelectric (TE) materials are attracting increasing attention in the materials research community as they allow for the direct conversion of waste heat into electricity, thereby improving the overall efficiency of power generation [1–4]. Typically, thermoelectric devices have been so far based on inorganic compounds, but also hybrid (organic-inorganic) TE materials have recently attracted the attention of many, in both the academic and industrial fields [5–9]. Indeed, considering the exponential increase in energy consumption, the possibility to recover electrical energy directly from lower-temperature waste heat using hybrid materials may represent a crucial advantage over inorganic ones [10]. Moreover, TE devices fed by the heat produced during metabolic processes are considered today a promising energy source for wearable electronics [1], such as fitness trackers, smartwatches, and medical sensors. This latter class of devices requires the simultaneous fulfilment of (at least) two conditions: a good TE efficiency and a suitable fitting to the human body (as films, patches, or clothes), as allowed by flexible TE materials. In this line, we foresee that hybrid TE materials, combining the good electrical transport properties of semiconducting transition metal dichalcogenides (TMDC) with the typically low thermal conductivity of organic compounds, might be considered promising candidates, particularly if the solution is processable and cast as thin films [3,11].

Our interest in TE applications of TMDC focuses on those species that crystallize in layered structures. In these cases, the basic stoichiometry is MX<sub>2</sub>, where M is a transition metal, and X is a chalcogen: S, Se, or Te. These materials consist of tightly and covalently bonded X-M-X stacks or sheets running normal to one crystal axis (usually taken as the *c*-direction); at variance, the stacking sequence and geometry are stabilized by weak(er) van der Waals (vdW) interactions between the highly polarizable X atoms of adjacent layers. For what it matters here, one of the most interesting properties of TMDC is their ability to act as

host lattices and, consequently, to interact with a wide variety of guest atoms or molecules to give rise to the formation of intercalation compounds [12–14]. Different synthetic methods for the preparation of such hybrids exist (liquid permeation, exfoliation, etc.), which have been beautifully reviewed by Guo et al. and Jung et al. [15,16]. Among layered TMDC, titanium disulfide ( $\text{TiS}_2$ , the archetype of 2D transition metal dichalcogenides) is a promising candidate for *n*-type thermoelectrics owing to some remarkable properties: it is chemically stable, mechanically manageable [17], and environmentally benign and contains earth-abundant elements (Ti and S).

Intercalation compounds of TMDC, where neutral organic molecules (NOM) are inserted in a regular or less ordered fashion, have been the subject of numerous studies [13,18–20]. However, many relevant aspects, such as stoichiometry, chemical stability, thermal inertness, polymorphic occurrence, or the nature of  $\text{MX}_2$ -NOM bonding, are still not completely clarified.

In this paper, we report the synthesis and both the physicochemical and the structural characterization of TMDC–alkylamine intercalation compounds obtained by a simple and reproducible, green and solventless mechanical grinding process, which fulfills the atom economy protocol [14,21].

Based on the experimental evidence of elemental sulfur formation from the  $\text{TiS}_2$ –hexylamine hybrid upon aging in environmental conditions (an obvious drawback for ambient use and exposure of this material), we present an *ab initio* DFT study and evaluate the formation enthalpy of the several species that could explain possible reaction paths toward the (undesired) formation of the crystalline (orthorhombic)  $\text{S}_8$  species. In this way, the most probable decomposition mechanism is pinpointed, paving the way for proper countermeasures to be taken into account for practical applications.

## 2. Materials and Methods

### 2.1. Synthesis

$\text{TiS}_2$  powder (99.8% metals basis, Alfa Aesar, Haverhill, MA, USA) and liquid *n*-hexylamine (99%, Sigma-Aldrich, St. Louis, MO, USA, labeled as HA in the following), combined in a 1:4 molar ratio, were mixed in an agate mortar and manually ground with a pestle for 30 min (Figure 1). This synthesis was found to be highly reproducible. After grinding, the volume of the powders expanded significantly, indicating that the intercalation was effective, with an evident color change from black to shiny brown. The intercalated hybrid is labeled as  $\text{TiS}_2/\text{HA}$  below. The pertinent chemical reaction then reads:

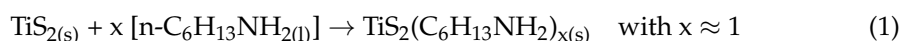


**Figure 1.** Scheme of the intercalation process through mechanochemical synthesis.

This material was found to be unstable if exposed for a prolonged time to environmental conditions. Indeed, we noticed that after 12 months storage without specific precautions,  $\text{TiS}_2/\text{HA}$  had gone through macroscopic changes. For this reason, the effect of aging on this sample was further investigated. Two batches of freshly prepared  $\text{TiS}_2/\text{HA}$  were left

for 1 week in different environments: one in air and the other in inert atmosphere ( $N_2$ ), both in the dark and at room temperature.

## 2.2. Experimental Characterization

X-ray powder diffraction (XRPD) data were acquired in Bragg–Brentano geometry on a Rigaku Miniflex 600 (Tokyo, Japan) or on a Bruker D8 Advance diffractometer (Billerica, MA, USA), both working in vertical scan using Ni-filtered  $Cu K_\alpha$  radiation. XRPD traces were analyzed with Topas [22], for peak hunting whole pattern profile analyses, in the structureless (Le Bail) or Rietveld modes (see Supplementary Materials for the full description of such analyses).

Thermogravimetric traces under nitrogen were acquired from room temperature to 700 °C using a TA Q500 thermogravimetric analyzer (New Castle, DE, USA) with a Pt sample holder. Micro-Raman spectra were recorded on a Horiba Raman Evolution spectrometer employing a confocal microscope with 50× long working distance and a laser with an excitation wavelength of 633 nm. Imaging by scanning electron microscopy (SEM) was performed in secondary electron mode using FEI Versa 3D (Lincoln, NE, USA) using a 10 kV acceleration voltage.

## 2.3. Computational Methods

Periodic ab initio DFT + U calculations were carried out with the PWscf package in the Quantum ESPRESSO 6.7 suite [23,24].  $TiS_2$  hybrids were modeled starting from the  $P-3m1$  trigonal parent structure, and enlarging the  $c$  lattice parameter to accommodate amines. All structures were fully relaxed, and energies were calculated using a  $k$ -space sampling over a dense  $8 \times 8 \times 4$  grid. The pseudopotentials and kinetic energy and density cut-offs were taken from the standard solid-state pseudopotential efficiency library (SSSP) [25,26]. All calculations were performed using the generalized gradient approximation [27] and the PBEsol exchange-correlation functional [28]. The value of Hubbard U parameter for the Ti atom was set to 3 eV [29]. The van der Waals interlayer interactions were considered using Grimme's D2 dispersion correction [30,31].

## 3. Results and Discussion

The macroscopic evidence of materials swelling during synthesis clearly indicated that hexylamine could be rapidly incorporated into  $TiS_2$  by a simple mechanochemical synthetic method. This unsophisticated method was indeed quantitative and could be repeated many times with the same outcome, providing robust information on its reproducibility. The structural changes were easily followed by acquiring X-ray powder diffraction (XRPD) data from the final product. In this sense, XRPD was first used in its qualitative (i.e., fingerprinting) mode, and when later used in a quantitative way, it allowed the determination of the axial  $d$ -spacings of the intercalated materials and for assessing either the presence of contaminant residues or the (unexpected) formation of elemental sulfur upon sample degradation. Specifically, in the pristine  $TiS_2$  solid, where  $Ti^{4+}$  ions are sandwiched between two sulfide layers, the 001 peak, corresponding to the stacking periodicity, falls near 15.7° (i.e., 5.69 Å). After 30 min grinding, when the macroscopic alterations exhibited by the powders (liquid amine absorbed, volume increment, and color change) indicated that the intercalation of hexylamine into  $TiS_2$  occurred, XRPD was used to monitor the changes in the interlayer distance between adjacent S-Ti-S sheets. In the  $TiS_2/HA$  species, the 001 peak in the XRD pattern (the strongest one in the traces shown in Figure 2) shifted from 15.7° to 4.1°. This implies an enormously increased ( $4\times$ ) separation between layers (21.6 Å) compared with that found on the pristine  $TiS_2$  (5.69 Å), confirming HA intercalation.

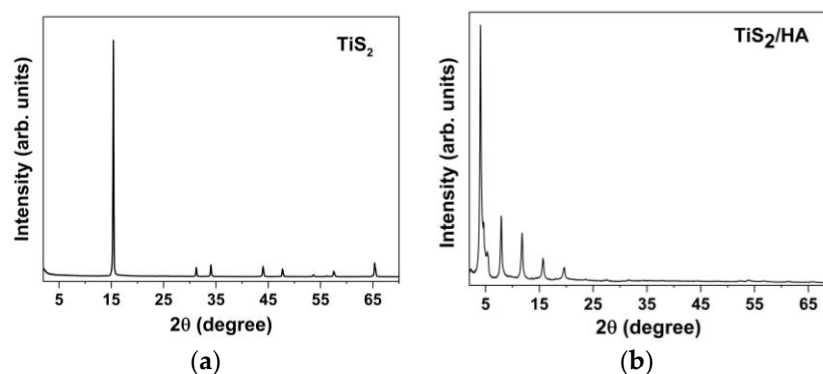


**Figure 2.** XRPD patterns of (a) pristine  $\text{TiS}_2$  and (b)  $\text{TiS}_2/\text{HA}$ .

It is worth noting that the stacking sequence in polymorphs and polytypes of intercalated  $\text{TiS}_2$  can be different, and is normally addressed by the occurrence of superstructure peaks, here not observed. However, since we detected peaks along only one reciprocal space rod ( $00l$ ), this technique may be fully blind to polymorphs occasionally sharing the same d-spacing along  $c$ . Thus, we cannot exclude that the  $\text{TiS}_2$  layers in the intercalated hybrids are slightly offset in the  $xy$  plane.

Considering the  $c$ -axis expansion (ca.  $15.9 \text{ \AA}$ ), we can safely conclude that HA was embedded into the  $\text{TiS}_2$  lattice, forming a bilayer structure. Since the estimated length of a single HA molecule, in its common all-trans conformation, H-bonded to S and van der Waals radii-corrected, is ca.  $11.5 \text{ \AA}$ , the limited increase of the  $c$ -axis value suggests that the intercalated molecules possess a measurable inclination in the van der Waals gap of  $\text{TiS}_2$ , being  $44^\circ$  the estimated angle:  $\sin^{-1}(15.9/(2 \times 11.5)) = 43.7^\circ$  (Figure 3). Our DFT computational analysis provided geometry optimization of the HA location and orientation, eventually leading to an inclination of  $40.0^\circ$ , in very good agreement with the purely geometrical consideration set above. Density and geometrical considerations also indicate that 100% filling of the interlayer separation requires a stoichiometric  $\text{TiS}_2/\text{HA}$  formulation (one amine per  $\text{TiS}_2$  unit formula), which, inter alia, would provide a cross-section area of ca.  $20.0 \text{ \AA}^2$ , like that found in the orthorhombic all-trans polyethylene crystal phase [32].

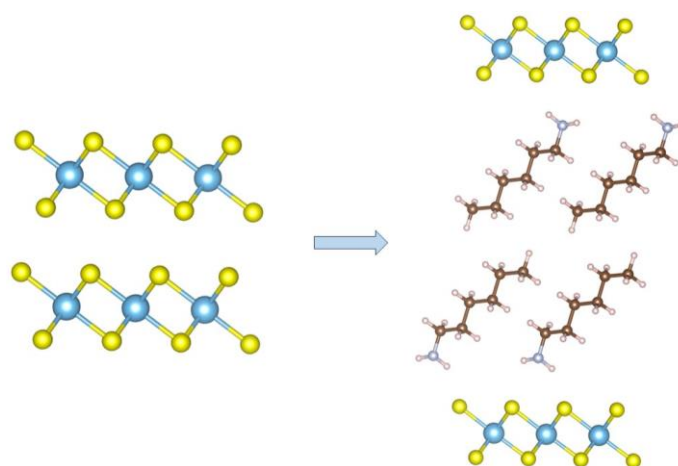


**Figure 3.** Left: crystal structure of pristine  $\text{TiS}_2$ . Right: proposed crystal structure of  $\text{TiS}_2/\text{HA}$ , containing one HA molecule per  $\text{TiS}_2$  formula unit.

Thermogravimetric studies (TGA) were performed to estimate the quantity of hexylamine in the inorganic matrix, through calculation of the molar coverage fraction (as mol/mol  $\text{TiS}_2$ ), defined as:

$$\frac{\Delta\%_{\text{org}} \times \text{MM}(\text{TiS}_2)}{\text{MM}(\text{HA}) \times (100 - \Delta\%_{\text{org}})} \quad (2)$$

where  $\Delta\%_{\text{org}}$  is the weight loss at 250 °C due to the organic moieties, and MM are the molar masses.

The weight loss of pristine  $\text{TiS}_2$  was 3.36%, which was subtracted from  $\Delta\%_{\text{org}}$ . To obtain a reproducible result, the sample was prepared and subjected to TGA analysis thrice. The average weight loss of the organic component was  $43.06 \pm 0.26\%$ . Then, the exact stoichiometry of the intercalated system sample was  $\text{TiS}_2(\text{HA})_{0.833}$ , not far from the  $\text{TiS}_2(\text{HA})$  formula used as a model for our DFT simulations (vide infra).

After 12 months of aging in the dark at environmental conditions, the XRPD pattern of powders of  $\text{TiS}_2/\text{HA}$  evidenced the limited stability of this intercalated material. Moreover, the formation of new crystalline phases was clearly observed. Indeed, jointly with residual  $\text{TiS}_2/\text{HA}$ , elemental sulfur was formed in its low-temperature/low-pressure orthorhombic polymorph (*Fddd* space group [33]). The complete Le Bail/single peak and Rietveld refinement plot for such sample, which contains  $\text{TiS}_2/\text{HA}$ , an unknown contaminant and crystalline sulfur, is shown in Figure 4.

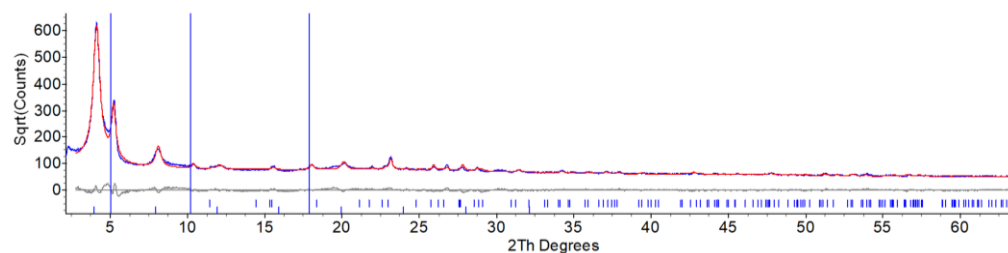


**Figure 4.** XRD pattern of 12-month-aged  $\text{TiS}_2/\text{HA}$ , showing the partial degradation of the intercalated material with the formation of crystalline sulfur. Data modeling of the polyphasic  $\text{TiS}_2/\text{HA}$  sample was performed by a hybrid approach comprising Rietveld refinement of rhombic sulfur and 1D structureless Le Bail refinement of the  $\text{TiS}_2/\text{HA}$  species. Blue trace: observed data; red trace, simulated pattern. Difference plot (in grey) and peak markers, for sulfur and 00l reflections belonging to the  $\text{TiS}_2/\text{HA}$  crystal phase (blue ticks), are drawn at the bottom. The three spurious peaks highlighted by the blue vertical lines are attributed to different HA packing (or content) and/or to unknown contaminants.

A puzzling and open question, however, remains: what is the fate of titanium atoms? As anticipated, sulfur exsolution is accompanied by the formation of an unknown and partially crystalline contaminant (see blue vertical lines in Figure 4). The few uninterpreted diffraction peaks do not match any titania polymorph, nor could they be related to any other reasonable reaction product, such as those presented in the computational study discussed below, with the obvious substitution of  $\text{NH}_{3-n}$  residues with  $\text{CH}_3(\text{CH}_2)_5\text{NH}_{2-n}$  ones ( $n = 0, 1, 2$ ). Additionally, the large incoherent scattering raising the overall background level suggests that noncrystalline components are present (amorphous titania and its congeners [34], to mention a few).

Further evidence of sulfur demixing is given by Raman spectroscopy. Figure 5 shows the Raman spectra of three samples: pristine  $\text{TiS}_2$  and  $\text{TiS}_2/\text{HA}$  (in the 200–500  $\text{cm}^{-1}$  range) and aged  $\text{TiS}_2/\text{HA}$  (20–500  $\text{cm}^{-1}$ ). As expected, the Raman spectrum of the as-prepared  $\text{TiS}_2/\text{HA}$  is very similar to that of pristine  $\text{TiS}_2$ , while the aged  $\text{TiS}_2/\text{HA}$  hybrid exhibits many more signals due to sulfur exsolution.

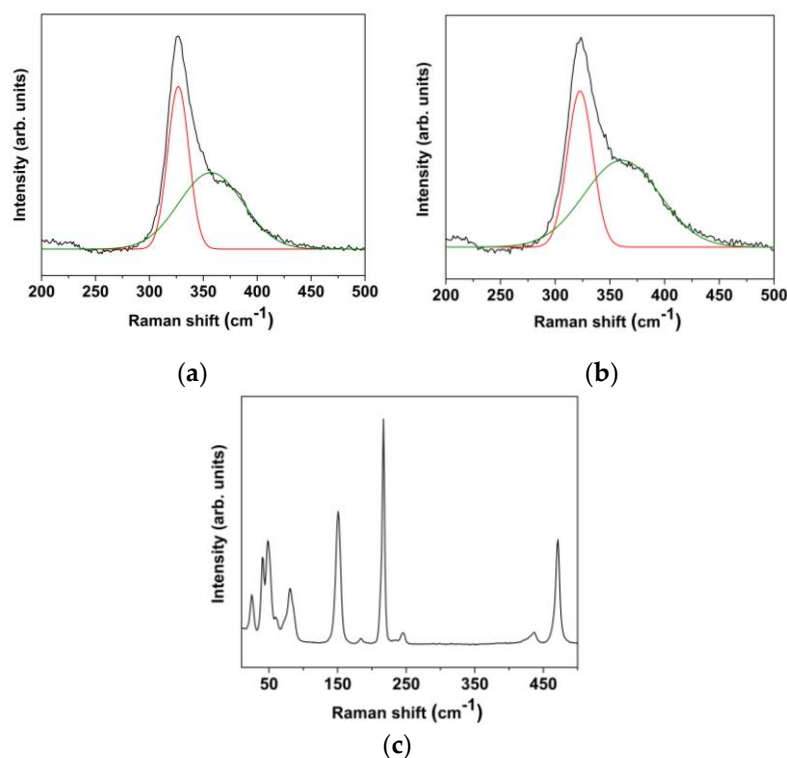


**Figure 5.** Micro-Raman spectra of (a) pristine  $\text{TiS}_2$ , (b)  $\text{TiS}_2/\text{HA}$ , and (c) aged  $\text{TiS}_2/\text{HA}$ . In panels (a,b), the deconvolution of the Raman peaks with two components is shown.

The phonon modes at the  $\Gamma$ -point of the reciprocal space can be probed by Raman and IR spectroscopies. The primitive cell of  $\text{TiS}_2$  consists of two chalcogen atoms and one metal atom with trigonal prismatic coordination, with the optical normal modes of vibration  $A_{1g}$ ,  $E_g$  (Raman active),  $A_{2u}$ , and  $E_u$  (IR active). The experimental Raman spectrum was then interpreted through simulation of the active modes (Table 1).

**Table 1.** Vibrational modes of  $\text{TiS}_2$  calculated by DFT + U simulations.

Mode	Raman Shift ( $\text{cm}^{-1}$ )
$E_u$	162.45
$E_g$	233.10
$A_{1g}$	321.23
$A_{2u}$	361.10

The calculated Raman shifts are in very good agreement with the experimental ones. In particular, the Raman-active mode out of the plane ( $A_{1g}$ ) is measured at  $326.9 \text{ cm}^{-1}$  for the pristine system, and  $322.7 \text{ cm}^{-1}$  for the intercalated one, confirming that the simulation captures well the electronic structure of the layered compound.

A high-energy shoulder peak located at  $\sim 360 \text{ cm}^{-1}$ , labeled Sh in the literature, is evident in the Raman spectra as an additional component (shown in Figure 6,  $\text{TiS}_2$  and  $\text{TiS}_2/\text{HA}$ ). Although this peak position matches the calculated frequency of the  $A_{2u}$  mode, it cannot be ascribed to this vibrational mode, the symmetry of which ( $A_{2u}$ ) makes it only IR active. The physical origin of this shoulder has been subject to several interpretations in the literature, but no general consensus has been reached to date [35–37]. Significantly, the presence of intercalated HA between the Ti-S layers does not affect the vibration modes in the measured range (see Figure 6).



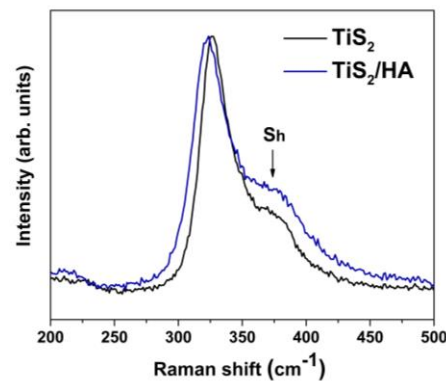


**Figure 6.** Comparison between the Micro-Raman spectra of pristine  $\text{TiS}_2$  (black) and of the intercalated  $\text{TiS}_2/\text{HA}$  hybrid (blue).

An interesting aspect of the change brought about by the intercalation process is the morphological evolution of the sample with time, evident at both the macroscopic and the microscopic scales. As Figure 7 shows, pristine  $\text{TiS}_2$  is a fine and dry black powder, while  $\text{TiS}_2/\text{HA}$  is a brown sticky powder, probably because of residual (not intercalated) hexylamine. Due to progressive material degradation, after 2 months,  $\text{TiS}_2/\text{HA}$  turns almost grey, and 1 year later, a yellow powder is found instead. The morphology of  $\text{TiS}_2$ , freshly prepared and aged (in air)  $\text{TiS}_2/\text{HA}$  hybrids, was also investigated using SEM imaging (Figure 8).

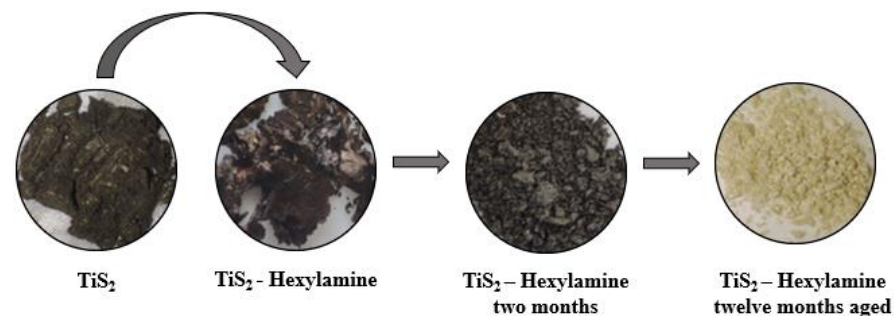


**Figure 7.** Macroscopic morphological and color changes of  $\text{TiS}_2/\text{HA}$ .

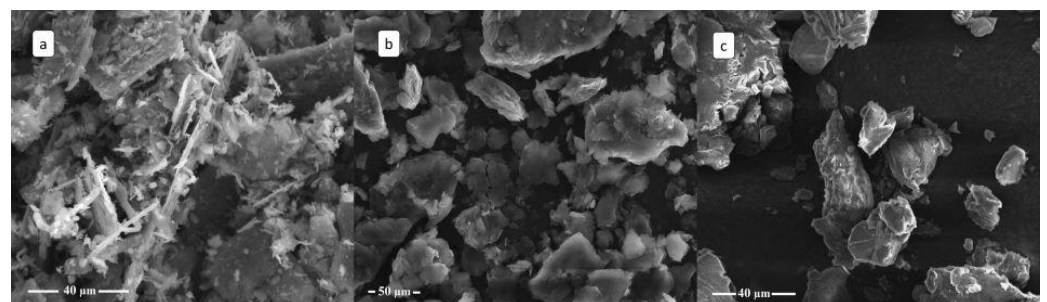


**Figure 8.** SEM images of (a) pristine  $\text{TiS}_2$ , (b) fresh  $\text{TiS}_2/\text{HA}$ , and (c) aged  $\text{TiS}_2/\text{HA}$ .

The SEM images of the intercalated compounds (both fresh and aged) show a substantial modification of the  $\text{TiS}_2$  morphology. In pristine  $\text{TiS}_2$ , the lamellar shape of the crystals is evident, but it fully disappears in the freshly prepared  $\text{TiS}_2/\text{HA}$  hybrid, demonstrating that the mechanical treatment induces a severe morphological change, where a simple topotactic HA insertion does not maintain crystal size and shapes, it being accompanied by a complete lamellar disruption. Estimation of the average crystal domain lengths (along c) from the peak broadening of XRPD data confirms that from micrometer-sized  $\text{TiS}_2$  crystals, coherent domains of average size as low as 40 nm are formed in  $\text{TiS}_2/\text{HA}$ . On the other

hand, there is no substantial microscopic modification upon aging, despite the occurrence of sulfur exsolution (with coherent isotropic domains of about 50 nm) and partial sample degradation. The hybrid structure, obtained by intercalation of the HA within the  $\text{TiS}_2$  lattice, remains stable even after partial sulfur elimination. The hypothesis is confirmed by the XRPD pattern reported above in Figure 4, as the persistence of the 001 peak of the intercalated compound is the dominating signal also upon material aging.

In order to pinpoint the driving force behind the decomposition of  $\text{TiS}_2/\text{HA}$ , and a possible mechanism for sulfur exsolution, we calculated the enthalpy variations of several possible reactions ( $\Delta H_r$ , as  $E(\text{products}) - E(\text{reactants})$ ) with the DFT + U scheme described above. As is standard practice in this kind of simulations, the difference in total energy of products and reactants is taken as an approximation of the enthalpy of reaction.

Initially, different sulfur-deficient  $\text{TiS}_2$  superstructures were modeled. Three progressively larger supercells were constructed, with a corresponding dilution of sulfur vacancies. These ideal structures are synoptically depicted in Figure 9. As shown in Table 2, the enthalpic cost for the formation of a sulfur vacancy decreases as the cell size increases, but in all cases, the formation of such vacant sites is never energetically favored per se. Using a simple linear extrapolation of the  $\Delta H_r$  with  $1/n$  plot (for the  $\text{Ti}_n\text{S}_m$  formulation), the energy required to form an infinitely diluted (neutral) S-vacancy in  $\text{TiS}_2$  at the bulk limit can be estimated to be ca. 2.2 eV.

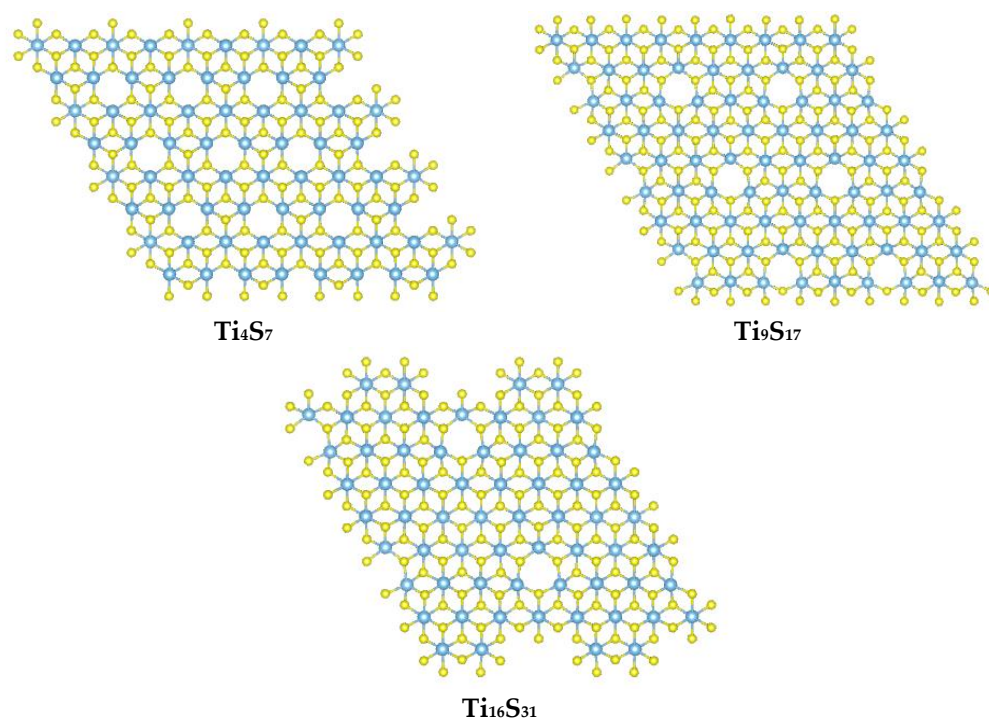


**Figure 9.** Top view of the different  $\text{TiS}_2$  supercells used in the DFT modeling, all with periodic sulfur vacant sites.

**Table 2.** Formation of sulfur defects in  $\text{TiS}_2$  at different concentrations (down to 0.03 at%). Extrapolation to an infinitely diluted vacant site leads to 2.2 eV, which is the energy required to eliminate one single (neutral) S atom from bulk  $\text{TiS}_2$ .

Reaction	$\Delta H_r$ (eV)
$\text{Ti}_4\text{S}_8 \rightarrow \text{Ti}_4\text{S}_7 + \text{S}$	3.14
$\text{Ti}_9\text{S}_{18} \rightarrow \text{Ti}_9\text{S}_{17} + \text{S}$	2.71
$\text{Ti}_{16}\text{S}_{32} \rightarrow \text{Ti}_{16}\text{S}_{31} + \text{S}$	2.43



Once the stability of pristine  $\text{TiS}_2$  was quantitatively confirmed, to understand and interpret the experimentally observed spontaneous intercalation of HA, we started considering two consecutive steps: (i) the formation of the  $\text{TiS}_2/\text{HA}$  hybrid and (ii) sulfur exsolution therefrom.

To reduce computational costs, we investigated the intercalation, within  $\text{TiS}_2$ , of simple amine molecules (using ammonia and methylamine instead of HA) (Table 3) with an idealized coverage of one nitrogen atom per four titanium ions (see Figure 10). Our calculations were then based on  $2 \times 2$   $\text{TiS}_2$  supercells with a single-side N-substitution. The intercalation reaction was mediated by moisture as amines or ammonia were used as aqueous solutions.

**Table 3.** Reaction energy of  $\text{TiS}_2$  intercalation compounds with either aqueous ammonia or aqueous methylamine.

Reaction	$\Delta H_r$ (eV)
$\text{Ti}_4\text{S}_8 + \text{NH}_4^+ + \text{OH}^- \rightarrow \text{Ti}_4\text{S}_8\text{NH}_3 + \text{H}_2\text{O}$	−2.93
$\text{Ti}_4\text{S}_8 + \text{CH}_3\text{NH}_3^+ + \text{OH}^- \rightarrow \text{Ti}_4\text{S}_8\text{CH}_3\text{NH}_2 + \text{H}_2\text{O}$	−1.75

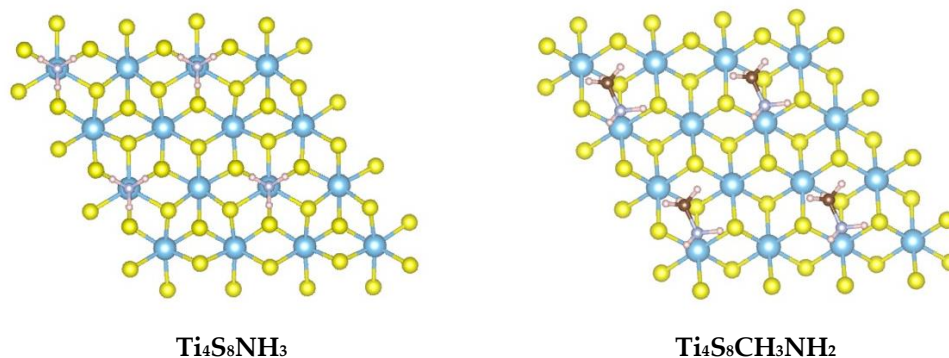


**Figure 10.** [001] view of  $\text{NH}_3$  and  $\text{CH}_3\text{NH}_2$  molecules adsorbed onto a  $\text{TiS}_2$  slab containing 16 metal atoms. Nitrogen atoms interact vertically with the Ti atoms of the  $\text{TiS}_2$  surface, with N . . . Ti distances of around 2.25 Å.

That the intercalation reaction, observed experimentally for hexylamine, is energetically favored is here confirmed by the simulated reaction energies, which are negative for both ammonia and methylamine cases. Once these adducts are formed, one sulfur atom is lost and nitrogen from the amine replaces it, with the formation of a Ti-N interaction. The fact that the  $\text{NH}_3$  molecule interacts favorably with Ti, replacing S in its position, suggests that the Ti-N bond formation may drive S exsolution. For this reason, a few different possible reactions were tested, all involving the formation of defective  $\text{TiS}_2$  slabs where amine groups carrying one to three H atoms actively interact with open Ti sites in close proximity to a sulfur vacancy. Some of these complexes are shown in the case of ammonia (Figure 11), where the S atom is replaced by N. A similar situation is obtained in the case of methylamine.

The last row in Table 4 indicates that the substitution of S by N is probably mediated by the action of molecular oxygen. In other words, the intercalated  $\text{TiS}_2/\text{amine}$  compounds seem to undergo sulfide oxidation to elemental sulfur, accompanied by a structural change in which Ti-N bonds are formed. In particular, the imido  $\text{Ti}_4\text{S}_7\text{NH}$  structure, where N is bound to three Ti sites, appears to be the most stable. Such  $\mu_3\text{-NH}$  coordination geometry on three Ti ions should not surprise, as it was found in a number of polynuclear organometallic complexes and, more paradigmatically, also in the highly symmetric  $[\text{Ti}(\text{NH})(\text{Cp}^*)]_4$  cubane ( $\text{Cp}^* = \text{tetramethyltrimethylsilylcyclopentadiene}$ ) [38].

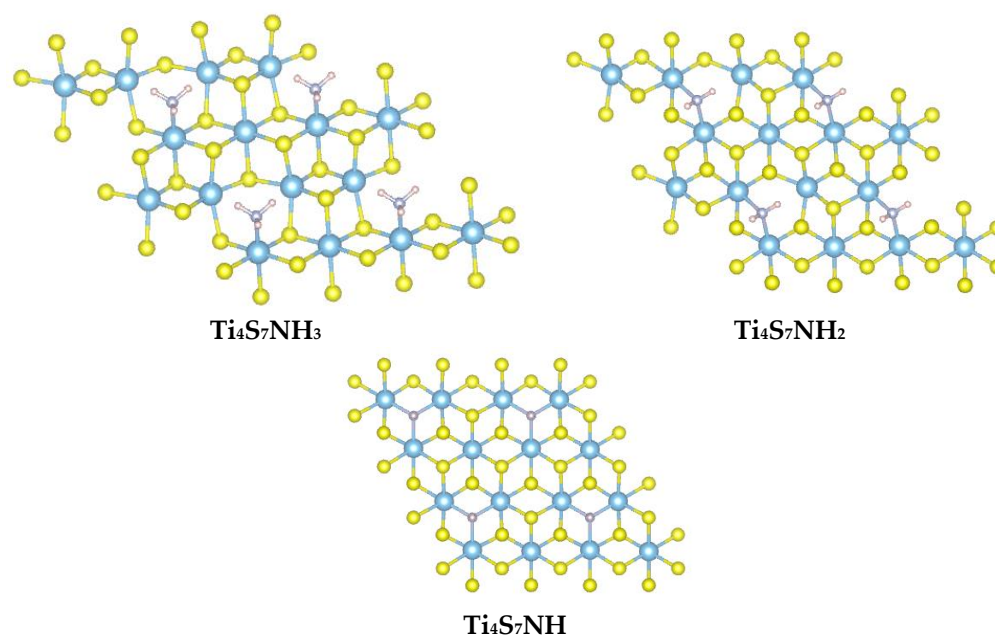


**Figure 11.** Top view of the nitrogen-containing Ti-S slabs formed by the loss of S atoms, substituted by ammonia molecules. In the last panel, all H atoms are eclipsed by N atoms, as N-H bonds lie perpendicular to the plane of drawing.

**Table 4.** Reaction energy of the formation of Ti-N bonds arising from the exsolution of S and its substitution with the (deprotonated) ammonia molecules.

Reaction	$\Delta H_r$ (eV)
$\text{Ti}_4\text{S}_8\text{NH}_3 \rightarrow \text{Ti}_4\text{S}_7\text{NH}_3 + \text{S}$	1.51
$\text{Ti}_4\text{S}_8\text{NH}_3 \rightarrow \text{Ti}_4\text{S}_7\text{NH}_2 + \text{S} + 1/2 \text{H}_2$	1.47
$\text{Ti}_4\text{S}_8\text{NH}_3 \rightarrow \text{Ti}_4\text{S}_7\text{NH} + \text{S} + \text{H}_2$	1.76
$\text{Ti}_4\text{S}_8\text{NH}_3 + 1/2 \text{O}_2 \rightarrow \text{Ti}_4\text{S}_7\text{NH} + \text{S} + \text{H}_2\text{O}$	-0.83

However, it should be noted that all four reactions reported in Table 4 are in principle consistent with the available experimental evidence (exsolution of crystalline sulfur). The impossibility of verifying experimentally which is the true path to sulfur elimination (which likely occurs very locally without the formation of a clearly distinguishable crystalline phase) makes uncertain the nature, stoichiometry, and structure of the newly formed Ti/S/N product.

In order to quantitatively assess the effective charge transfer between N and Ti, the electron densities (in the form of Bader charges [39,40]) of pristine  $\text{TiS}_2$  and different Ti-N complex supercells were compared (Table 5). By comparing bound structures with varying amounts of H atoms, it is seen that the Ti-N charge transfer is more and more effective as the amine group loses hydrogen atoms and forms stronger bonds with titanium: the Ti electron density decreases and the N/H electron density increases.

To experimentally test the hypothesis that the structural change (and material decomposition) of  $\text{TiS}_2/\text{HA}$  was a consequence of exposure to molecular oxygen, a newly prepared batch of  $\text{TiS}_2/\text{HA}$  was kept under inert atmosphere, while another batch was kept in air for comparison (both in the dark and at room temperature, for 1 week). Figure 12 compares the XRPD patterns of these two samples. The absence of crystalline sulfur in the case of  $\text{TiS}_2/\text{HA}$  kept in inert atmosphere is the experimental confirmation of the proposed reaction pathway, where  $\text{O}_2$  actively participates in sulfur elimination.

**Table 5.** Bader charges of  $\text{TiS}_2$  supercell and the Ti-N supercells formed via sulfur exsolution and substitution with nitrogen. The number of electrons explicitly included in the calculation is indicated for each element.

	$\text{Ti}_4\text{S}_8$	$\text{Ti}_4\text{S}_7\text{NH}_3$	$\text{Ti}_4\text{S}_7\text{NH}_2$	$\text{Ti}_4\text{S}_7\text{NH}$
Ti (10)	10.23	10.2721	10.1974	10.1304
S (8)	6.89	6.9950	6.9530	6.9218
N (7)	-	6.2964	6.3866	6.4353
H (1)	-	0.5500	0.5760	0.5900
Total Ti/S	96.00	90.05	89.46	88.97
Total ammonia	-	7.95	7.54	7.03
Total	96.00	98.00	97.00	96.00

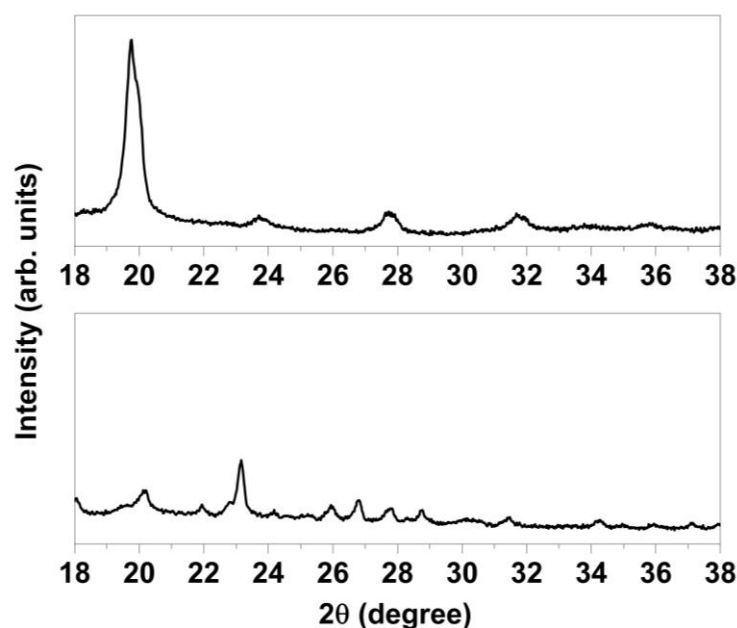


**Figure 12.** XRPD patterns of  $\text{TiS}_2/\text{HA}$  ( $\text{N}_2$ ) (top) and  $\text{TiS}_2/\text{HA}$  (air) (bottom), showing that sulfur exsolution only occurs by exposure to molecular oxygen.

#### 4. Conclusions

We report experimental evidence of limited stability in ambient conditions of hexylamine-intercalated titanium disulfide, a material that has recently attracted interest for prospected thermoelectric applications. X-ray powder diffraction and Raman spectroscopy clearly show the formation of crystalline sulfur at the expense of the layered  $\text{TiS}_2$ /hexylamine compound. Different degradation mechanisms were tested by ab initio periodic DFT calculations on a  $\text{TiS}_2/\text{NH}_3$  model system, suggesting that  $\text{TiS}_2$  reacts with molecular oxygen, resulting in Ti-N adducts, where N resides in lieu of S vacancies, with the subsequent formation of elemental sulfur and water. A comparison of the aging of  $\text{TiS}_2/\text{HA}$  in the presence or the absence of oxygen further corroborates the proposed mechanism, since prolonged storage in inert atmosphere does not result in the degradation of the intercalated material. Since our findings point to a limited stability in air of such hybrid systems, appropriate actions taken to minimize exposure to oxygen in practical applications should be devised for TMDC to be used in environmental conditions. While this appears to be a severe limitation for their wide usage, similar issues have been recently solved for oxygen- and moisture-labile hybrid materials (lead halide perovskites, above all [41]), which are deposited within thin layers of nonpermeable, and optically transparent, plastic films.

**Supplementary Materials:** The following supporting information can be downloaded at: <https://www.mdpi.com/article/10.3390/ma15238297/s1>, Figure S1: Rietveld refinement of the pristine  $\text{TiS}_2$

material; Figure S2: Structureless 1D Le Bail refinement of TiS<sub>2</sub>/HA hybrid with 001 peaks only; Figure S3: Structureless 1D Le Bail refinement of TiS<sub>2</sub>/HA (N<sub>2</sub>).

**Author Contributions:** Conceptualization and funding acquisition, N.M., A.M. and F.G.; investigation, F.U., S.V. and G.G.-E.; data curation, F.U. and N.M.; writing—original draft preparation, F.U.; writing—review and editing, G.G.-E., N.M. and F.G. All authors have read and agreed to the published version of the manuscript.

**Funding:** This project was partially supported by MIUR (PRIN-2017L8WW48, Project HY-TEC). We acknowledge the CINECA award under the ISCRA initiative for the availability of high-performance computing resources and support (projects IsC98\_DoC and IsC91\_DoPe).

**Institutional Review Board Statement:** Not applicable.

**Informed Consent Statement:** Not applicable.

**Data Availability Statement:** The data presented in this study are available on request from the corresponding author.

**Acknowledgments:** We thank S. Agnello (Università di Palermo) for the assistance during the Raman experiments and G. Nasillo (Electron Microscopy Lab, ATEN Center, Università di Palermo) for the SEM-EDS analyses.

**Conflicts of Interest:** The authors declare no conflict of interest.

## References

1. Newby, S.; Mirihanage, W.; Fernando, A. Recent Advancements in Thermoelectric Generators for Smart Textile Application. *Mater. Today Commun.* **2022**, *33*, 104585. [\[CrossRef\]](#)
2. Sun, W.; Liu, W.-D.; Liu, Q.; Chen, Z.G. Advances in Thermoelectric Devices for Localized Cooling. *Chem. Eng. J.* **2022**, *450*, 138389. [\[CrossRef\]](#)
3. Liu, Y.; Wang, W.; Yang, J.; Li, S. Recent Advances of Layered Thermoelectric Materials. *Adv. Sustain. Syst.* **2018**, *2*, 1800046. [\[CrossRef\]](#)
4. Gayner, C.; Kar, K.K. Recent Advances in Thermoelectric Materials. *Prog. Mater. Sci.* **2016**, *83*, 330–382. [\[CrossRef\]](#)
5. Cao, T.; Shi, X.L.; Chen, Z.G. Advances in the Design and Assembly of Flexible Thermoelectric Device. *Prog. Mater. Sci.* **2022**, *131*, 101003. [\[CrossRef\]](#)
6. Choi, J.; Gordon, M.P.; Yuan, P.; Kang, H.; Zaia, E.W.; Urban, J.J.; Li, L.; Lu, N.; Liu, M.; Xu, H.; et al. *Organic Thermoelectric Materials*; Lin, Z., He, M., Eds.; The Royal Society of Chemistry: London, UK, 2020; pp. 1–316, ISBN 978-1-78801-470-0.
7. Wang, H.; Yu, C. Organic Thermoelectrics: Materials Preparation, Performance Optimization, and Device Integration. *Joule* **2019**, *3*, 53–80. [\[CrossRef\]](#)
8. Cowen, L.M.; Atoyo, J.; Carnie, M.J.; Baran, D.; Schroeder, B.C. Review—Organic Materials for Thermoelectric Energy Generation. *ECS J. Solid State Sci. Technol.* **2017**, *6*, N3080–N3088. [\[CrossRef\]](#)
9. Champier, D. Thermoelectric Generators: A Review of Applications. *Energy Convers. Manag.* **2017**, *140*, 167–181. [\[CrossRef\]](#)
10. Jin, H.; Li, J.; Iocozzia, J.; Zeng, X.; Wei, P.; Yang, C.; Li, N.; Liu, Z.; He, J.H.; Zhu, T.; et al. Hybride Organisch-anorganische Thermoelektrische Materialien Und Baueinheiten. *Angew. Chem.* **2019**, *131*, 15348–15370. [\[CrossRef\]](#)
11. Huang, Y.; Liang, J.; Wang, C.; Yin, S.; Fu, W.; Zhu, H.; Wan, C. Hybrid Superlattices of Two-Dimensional Materials and Organics. *Chem. Soc. Rev.* **2020**, *49*, 6866–6883. [\[CrossRef\]](#)
12. Tchitchekova, D.S.; Ponrouch, A.; Verrelli, R.; Broux, T.; Frontera, C.; Sorrentino, A.; Bardé, F.; Biskup, N.; Arroyo-De Dompablo, M.E.; Palacín, M.R. Electrochemical Intercalation of Calcium and Magnesium in TiS<sub>2</sub>: Fundamental Studies Related to Multivalent Battery Applications. *Chem. Mater.* **2018**, *30*, 847–856. [\[CrossRef\]](#)
13. Tian, R.; Wan, C.; Wang, Y.; Wei, Q.; Ishida, T.; Yamamoto, A.; Tsuruta, A.; Shin, W.; Li, S.; Koumoto, K. A Solution-Processed TiS<sub>2</sub>/Organic Hybrid Superlattice Film towards Flexible Thermoelectric Devices. *J. Mater. Chem. A* **2017**, *5*, 564–570. [\[CrossRef\]](#)
14. Wan, C.; Tian, R.; Azizi, A.B.; Huang, Y.; Wei, Q.; Sasai, R.; Wasusate, S.; Ishida, T.; Koumoto, K. Flexible Thermoelectric Foil for Wearable Energy Harvesting. *Nano Energy* **2016**, *30*, 840–845. [\[CrossRef\]](#)
15. Guo, Z.; Sun, F.; Yuan, W. Chemical Intercalations in Layered Transition Metal Chalcogenides: Syntheses, Structures, and Related Properties. *Cryst. Growth Des.* **2017**, *17*, 2238–2253. [\[CrossRef\]](#)
16. Jung, Y.; Zhou, Y.; Cha, J.J. Intercalation in Two-Dimensional Transition Metal Chalcogenides. *Inorg. Chem. Front.* **2016**, *3*, 452–463. [\[CrossRef\]](#)
17. Commins, P.; Dippenaar, A.B.; Li, L.; Hara, H.; Haynes, D.A.; Naumov, P. Mechanically Compliant Single Crystals of a Stable Organic Radical. *Chem. Sci.* **2021**, *12*, 6188–6193. [\[CrossRef\]](#)
18. Wan, C.; Wang, Y.; Wang, N.; Norimatsu, W.; Kusunoki, M.; Koumoto, K. Development of Novel Thermoelectric Materials by Reduction of Lattice Thermal Conductivity. *Sci. Technol. Adv. Mater.* **2010**, *11*, 044306. [\[CrossRef\]](#)

19. Wan, C.; Tian, R.; Kondou, M.; Yang, R.; Zong, P.; Koumoto, K. Ultrahigh Thermoelectric Power Factor in Flexible Hybrid Inorganic–Organic Superlattice. *Nat. Commun.* **2017**, *8*, 1024. [[CrossRef](#)]
20. Wan, C.; Gu, X.; Dang, F.; Itoh, T.; Wang, Y.; Sasaki, H.; Kondo, M.; Koga, K.; Yabuki, K.; Snyder, G.J.; et al. Flexible N-Type Thermoelectric Materials by Organic Intercalation of Layered Transition Metal Dichalcogenide  $\text{TiS}_2$ . *Nat. Mater.* **2015**, *14*, 622–627. [[CrossRef](#)]
21. Trost, B.M. Atom Economy—A Challenge for Organic Synthesis: Homogeneous Catalysis Leads the Way. *Angew. Chem. Int. Ed. English* **1995**, *34*, 259–281. [[CrossRef](#)]
22. Coelho, A.A. TOPAS and TOPAS-Academic: An Optimization Program Integrating Computer Algebra and Crystallographic Objects Written in C++. *J. Appl. Crystallogr.* **2018**, *51*, 210–218. [[CrossRef](#)]
23. Giannozzi, P.; Baroni, S.; Bonini, N.; Calandra, M.; Car, R.; Cavazzoni, C.; Ceresoli, D.; Chiarotti, G.L.; Cococcioni, M.; Dabo, I.; et al. QUANTUM ESPRESSO: A Modular and Open-Source Software Project for Quantum Simulations of Materials. *J. Phys. Condens. Matter* **2009**, *21*, 395502. [[CrossRef](#)] [[PubMed](#)]
24. Giannozzi, P.; Andreussi, O.; Brumme, T.; Bunau, O.; Nardelli, M.B.; Calandra, M.; Car, R.; Cavazzoni, C.; Ceresoli, D.; Cococcioni, M. Advanced capabilities for materials modelling with Quantum ESPRESSO. *J. Phys. Condens. Matter* **2017**, *29*, 465901. [[CrossRef](#)] [[PubMed](#)]
25. Prandini, G.; Marrazzo, A.; Castelli, I.E.; Mounet, N.; Marzari, N. Precision and Efficiency in Solid-State Pseudopotential Calculations. *npj Comput. Mater.* **2018**, *4*, 72. [[CrossRef](#)]
26. Lejaeghere, K.; Bihlmayer, G.; Björkman, T.; Blaha, P.; Blügel, S.; Blum, V.; Caliste, D.; Castelli, I.E.; Clark, S.J.; Dal Corso, A.; et al. Reproducibility in Density Functional Theory Calculations of Solids. *Science* **2016**, *351*, 6280. [[CrossRef](#)] [[PubMed](#)]
27. Perdew, J.P.; Burke, K.; Ernzerhof, M. Generalized Gradient Approximation Made Simple. *Phys. Rev. Lett.* **1996**, *77*, 3865–3868. [[CrossRef](#)] [[PubMed](#)]
28. Perdew, J.P.; Ruzsinszky, A.; Csonka, G.I.; Vydrov, O.A.; Scuseria, G.E.; Constantin, L.A.; Zhou, X.; Burke, K. Restoring the Density-Gradient Expansion for Exchange in Solids and Surfaces. *Phys. Rev. Lett.* **2008**, *100*, 136406. [[CrossRef](#)] [[PubMed](#)]
29. Hubbard, J. Electron Correlations in Narrow Energy Bands. *Proc. R. Soc. Lond. Ser. A Math. Phys. Sci.* **1963**, *276*, 238–257. [[CrossRef](#)]
30. Grimme, S.; Ehrlich, S.; Goerigk, L. Effect of the Damping Function in Dispersion Corrected Density Functional Theory. *J. Comput. Chem.* **2011**, *32*, 1456–1465. [[CrossRef](#)]
31. Grimme, S.; Antony, J.; Ehrlich, S.; Krieg, H. A Consistent and Accurate Ab Initio Parametrization of Density Functional Dispersion Correction (DFT-D) for the 94 Elements H–Pu. *J. Chem. Phys.* **2010**, *132*, 154104. [[CrossRef](#)]
32. Bunn, C.W. The crystal structure of long-chain normal paraffin hydrocarbons. The “shape” of the  $\text{<CH}_2$  group. *Trans. Faraday Soc.* **1939**, *35*, 482–491. [[CrossRef](#)]
33. Mikuriya, M.; Taniguchi, K.; Koyama, Y.; Watanabe, H.; Yoshioka, D.; Mitsuhashi, R.; Asato, E. Crystal Structure of S8 Molecule from Thiourea. *X-ray Struct. Anal. Online* **2020**, *36*, 1–2. [[CrossRef](#)]
34. Grey, I.E.; Bordet, P.; Wilson, N.C. Structure of the Amorphous Titania Precursor Phase of N-Doped Photocatalysts. *RSC Adv.* **2021**, *11*, 8619–8627. [[CrossRef](#)]
35. Sherrell, P.C.; Sharda, K.; Grotta, C.; Ranalli, J.; Sokolikova, M.S.; Pesci, F.M.; Palczynski, P.; Bemmer, V.L.; Mattevi, C. Thickness-Dependent Characterization of Chemically Exfoliated  $\text{TiS}_2$  Nanosheets. *ACS Omega* **2018**, *3*, 8655–8662. [[CrossRef](#)] [[PubMed](#)]
36. Dużyńska, A.; Judek, J.; Wilczyński, K.; Zborecki, K.; Łapińska, A.; Wróblewska, A.; Zdrojek, M. Temperature-Induced Phonon Behavior in Titanium Disulfide ( $\text{TiS}_2$ ) Nanosheets. *J. Raman Spectrosc.* **2019**, *50*, 1114–1119. [[CrossRef](#)]
37. Lin, C.; Zhu, X.; Feng, J.; Wu, C.; Hu, S.; Peng, J.; Guo, Y.; Peng, L.; Zhao, J.; Huang, J.; et al. Hydrogen-Incorporated  $\text{TiS}_2$  Ultrathin Nanosheets with Ultrahigh Conductivity for Stamp-Transferrable Electrodes. *J. Am. Chem. Soc.* **2013**, *135*, 5144–5151. [[CrossRef](#)] [[PubMed](#)]
38. Shima, T.; Luo, G.; Hu, S.; Luo, Y.; Hou, Z. Experimental and Computational Studies of Dinitrogen Activation and Hydrogenation at a Tetranuclear Titanium Imide/Hydride Framework. *J. Am. Chem. Soc.* **2019**, *141*, 2713–2720. [[CrossRef](#)]
39. Tang, W.; Sanville, E.; Henkelman, G. A Grid-Based Bader Analysis Algorithm without Lattice Bias. *J. Phys. Condens. Matter* **2009**, *21*, 084204. [[CrossRef](#)]
40. Henkelman, G.; Arnaldsson, A.; Jónsson, H. A Fast and Robust Algorithm for Bader Decomposition of Charge Density. *Comput. Mater. Sci.* **2006**, *36*, 354–360. [[CrossRef](#)]
41. Wang, Z.; Jin, J.; Zheng, Y.; Zhang, X.; Zhu, Z.; Zhou, Y.; Cui, X.; Li, J.; Shang, M.; Zhao, X.; et al. Achieving Efficient and Stable Perovskite Solar Cells in Ambient Air Through Non-Halide Engineering. *Adv. Energy Mater.* **2021**, *11*, 2102169. [[CrossRef](#)]